





Cite this: *Phys. Chem. Chem. Phys.*,  
2024, 26, 12947

# Prediction of superhard $C_{1+x}N_{1-x}$ compounds with metal-free magnetism and narrow band gaps

Haiping Wu, <sup>†\*ab</sup> Yunhao Zheng,<sup>†a</sup> Erjun Kan <sup>ab</sup> and Yan Qian<sup>\*ab</sup>

The scarcity of superhard materials with magnetism or a narrow band gap, despite their potential applications in various fields, makes it desirable to design such materials. Here, a series of  $C_{1+x}N_{1-x}$  compounds are theoretically designed by replacing different numbers of nitrogen atoms with carbon atoms in the synthesized  $C_1N_1$  compound. The results indicate that the compounds  $C_5N_3$  and  $C_7N_1$  possess both superhardness and antiferromagnetic ordering due to the introduction of low-coordinated carbon atoms. The hardness of the two compounds is about 40.3 and 54.5 GPa, respectively. The magnetism in both compounds is attributed to the unpaired electrons in low-coordinated carbon atoms, and the magnetic moments are 0.42 and 0.39  $\mu_B$ , respectively. Interestingly, the magnetism in  $C_5N_3$  remains unaffected by the external pressure used in this study, whereas  $C_7N_1$  becomes nonmagnetic when the pressure exceeds  $\sim 80$  GPa. Electronic calculations reveal that both compounds behave as indirect band gap semiconductors, with narrow energy gaps of about 0.30 and 0.20 eV, respectively. Additionally, the other two compounds,  $C_6N_2$ -I and  $C_6N_2$ -III, exhibit nonmagnetic ordering and possess hardness values of 52.6 and 35.0 GPa, respectively.  $C_6N_2$ -I behaves as a semiconductor with an energy gap of 0.79 eV, and  $C_6N_2$ -III shows metallic behavior. Notably, the energy gaps of  $C_5N_3$  and  $C_6N_2$ -I remain nearly constant under arbitrary pressure due to their porous and superhard structure. These compounds fill the gap in magnetic or narrow band gap superhard materials, and they can be used in the spintronic or optoelectronic fields where conventional superhard materials are not suitable.

Received 19th January 2024,  
Accepted 8th April 2024

DOI: 10.1039/d4cp00256c

rsc.li/pccp

## 1. Introduction

Superhard materials, which possess high Vickers hardness ( $H_V$ ) ( $> 40$  GPa),<sup>1</sup> play a crucial role in contemporary industries. Consequently, they have been widely used in diverse fields,<sup>2,3</sup> such as cutting and polishing tools, wear-resistant coatings, *etc.* However, superhard materials that have been commercially applied are scarce yet. Carbon diamond and cubic boron nitride (c-BN) are the only two of them, and they have  $H_V$  of  $\sim 100$  and 33–45 GPa,<sup>4,5</sup> respectively. The two materials, however, have their limitations. For example, diamond exhibits inferior thermal stability and chemically reacts with ferrous metals when subjected to extremely high pressure, and c-BN shows relatively low hardness and is prohibitively expensive due to the extreme conditions required for synthesis.

The high hardness of materials is primarily attributed to the presence of strong covalent bonds. Moreover, the strong covalent bonds usually result in the semiconducting or insulating

properties of superhard materials. For example, both carbon diamond and c-BN exhibit insulating properties, with band gaps of 5.47 and 6.40 eV, respectively. However, the unique electronic properties hinder the applications of superhard materials to many other fields, such as hard coatings in electromechanical systems, special wear-resistant parts, electronic applications under high stress, *etc.* Additionally, magnetism also plays an important role in technological applications, for example, data storage, gap sensors utilizing the change of magnetism,<sup>6,7</sup> and so on. Unfortunately, superhard materials with magnetism are rarely reported, especially those consisting of lightweight elements (*e.g.*, B, C, O, and N). This case hinders their applications in some special fields, such as magnetic bearings, magnetic rotors, *etc.*

Compounds composed of lightweight elements typically exhibit superhard properties due to the formation of strong and short bonds. For example, several superhard  $C_3N_4$  compounds, with hardness ranging from 62.3 to 92.0 GPa, have been reported,<sup>8–14</sup> although the structures of the synthesized  $C_3N_4$  allotropes are still being debated due to the limited quantity and heterogeneity of samples. Notably, the hardness of certain  $C_3N_4$  compounds closely approaches that of diamond. It was also suggested that there are thermodynamically favorable C–N compounds (with different C/N ratios) in

<sup>a</sup> School of Physics, Nanjing University of Science and Technology, Nanjing 210094, China. E-mail: mrhpwu@njut.edu.cn, qianyan@njut.edu.cn

<sup>b</sup> MIT Key Laboratory of Semiconductor Microstructure and Quantum Sensing, Nanjing University of Science and Technology, Nanjing 210094, China

<sup>†</sup> Haiping Wu and Yunhao Zheng contributed equally to this work.

comparison to  $C_3N_4$ . Inspired by this case, the C–N binary compounds gained great attention as potential rivals to diamond in terms of hardness. Subsequently, a series of superhard C–N compounds with superhard properties were explored by many researchers, for instance, semiconducting  $Pnnm$ -CN with a  $H_v$  of 62.3 GPa,<sup>15</sup> semiconducting  $\alpha$ - $C_3N_2$  and  $\beta$ - $C_3N_2$  having a  $H_v$  of 86 GPa,<sup>16</sup> a simple cubic structure  $C_4N$  with a  $H_v$  of 40.1 GPa and several  $C_{17}N_4$  systems with a  $H_v$  of 64.0 GPa,<sup>17</sup> a direct band gap semiconducting  $C_5N_2$  ( $H_v = 74.9$  GPa) and antiferromagnetic  $C_4N_3$  ( $H_v = 54.4$  GPa) predicted recently,<sup>18,19</sup> and so on. Notably, the reported superhard C–N compounds are mainly limited to carbon rich systems (*i.e.*, the nitrogen content lower than 50%), in that the synthesis of nitrogen-rich compounds is not beneficial due to the strong repulsions between nitrogen atoms caused by short nonbonded distances. Moreover, the aforementioned compounds are primarily reported through theoretical calculations.

Recently, the  $Pnnm$   $C_1N_1$  compound, which has been theoretically predicted by Wang,<sup>15</sup> was synthesized using laser-heating technology under high external pressures. Tetracyanoethylene mixed with  $N_2$  or graphite mixed with  $N_2$  was chosen as the precursor by two research groups, respectively.<sup>8,20</sup> Interestingly, one of the experimental studies, which utilized graphite and  $N_2$  as precursors, shows that diamond would be the sole product when quenched to room temperature at pressures above 70 GPa.<sup>20</sup> This result suggests the possibility of synthesizing other C–N compounds between  $C_1N_1$  and diamond (*i.e.*, the C:N ratio from 1 to  $\infty$ ) under different experimental conditions. Additionally, the C and N atoms in the synthesized  $C_1N_1$  compound are coordinated in a four-fold and three-fold manner, respectively. Therefore, substituting some N atoms with C atoms may result in the presence of unpaired electrons within the system, potentially leading to the emergence of magnetism.

Based on the above fact and using first-principles calculations, we studied a series of  $C_{1+x}N_{1-x}$  by replacing different numbers of N atoms with C atoms in the  $C_1N_1$  system. As expected, several superhard  $C_{1+x}N_{1-x}$  compounds with unique magnetic and electronic properties are predicted.

## 2. Computational methods

First-principles calculations employed in this work are executed using the VASP code.<sup>21</sup> The calculations are performed using generalized-gradient approximations with the Perdew–Burke–Ernzerhof (PBE) exchange–correlation functional and projector augmented wave (PAW) potentials.<sup>22,23</sup> The structures are relaxed until the Hellmann–Feynman force on each atom falls below  $0.001 \text{ eV } \text{\AA}^{-1}$ . The cutoff energy for the plane wave is set to be 500 eV, the total energy change is less than  $10^{-6} \text{ eV}$ , and Monkhorst–Pack  $k$ -point grids with a size of  $9 \times 11 \times 21$  are utilized for integrating the Brillouin-zone (BZ) in the first BZ. Since  $C_1N_1$  and diamond were synthesized at different pressures, the structural relaxations are performed at the initial step under pressures of 0 and 70 GPa, respectively. The phonon

dispersion is calculated by employing the supercell approach and the force-constant method. The force constants in real space for the supercells are determined using density functional perturbation theory (DFPT),<sup>24</sup> and then the PHONOPY code<sup>25,26</sup> is utilized to calculate the phonon dispersions.

## 3. Results and discussion

It was reported experimentally that diamond was the only product synthesized at a pressure of 70 GPa.<sup>20</sup> Therefore, the structure of  $C_{1+x}N_{1-x}$  with all N atoms replaced by C atoms is explored first. During the structural relaxations, two hydrostatic pressures of 0 and 70 GPa are used to simulate the synthesis conditions in the experiment. The results indicate that under pressures of 0 and 70 GPa, the system undergoes a transformation into graphite and diamond, respectively. The result is consistent with the experimental results,<sup>20</sup> and Fig. 1 illustrates the transformation process under two distinct pressures. In detail,  $Pnnm$   $C_1N_1$  could be regarded as the stacked 2D  $C_1N_1$  nanosheets that are covalently bonded to each other through C–C bonds (as drawn in Fig. 1(c) and (d)). As the pressure increases, carbon atoms may prefer to replace nitrogen atoms. After replacing all N atoms with C atoms, the structure of  $C_8N_0$  (named as  $C_8$ ) could be regarded as the stacked graphene layers with buckling characteristic. As long as the pressure is high enough to overcome a high

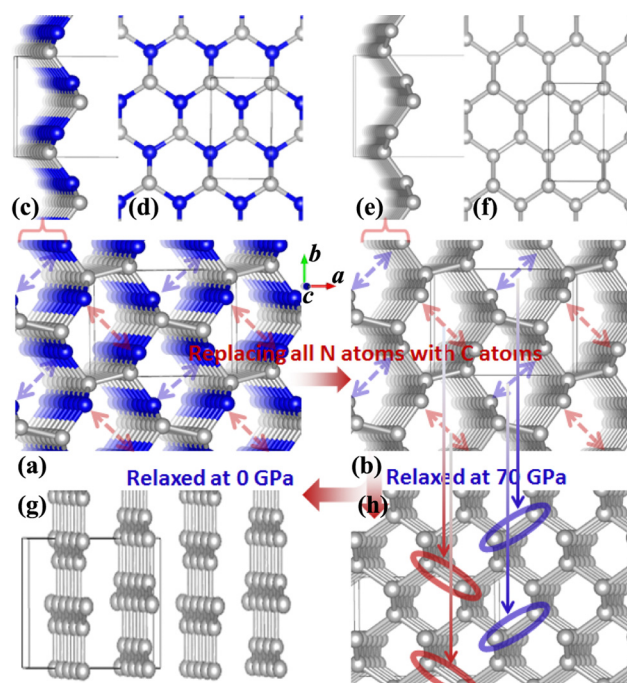


**Fig. 1** (a) The structure of  $Pnnm$   $C_1N_1$ . (b) The initial structure of  $Pnnm$   $C_1N_1$  after replacing all N atoms with C atoms (named as  $C_8$ ). (c) and (d) The side and top views of the monolayer  $C_1N_1$  exfoliated from the bulk  $Pnnm$   $C_1N_1$ . (e) and (f) The side and top views of the monolayer  $C_8$  exfoliated from the initial bulk  $Pnnm$   $C_8$ . (g) and (h) The optimized structures of the bulk  $Pnnm$   $C_8$  under the hydrostatic pressures of 0 and 70 GPa, respectively. The blue and brown spheres represent N and C atoms, respectively.

activation barrier, interlayer covalent bonds will be formed between the initial three-fold coordinated C atoms (the corresponding atoms forming bonds are indicated by red and blue arrows in Fig. 1(b), and the formed bonds are represented by red and blue ellipses in Fig. 1(h)), resulting in the transformation from the stacked graphene sheets to diamond. The transformation pressure is closely related to the stacking sequence of graphene layers,<sup>27,28</sup> in that the height of the energy barrier deeply depends on the starting structure. Moreover, different experimental technologies are another significant factor that profoundly affects the transformation pressure. For example, the pressure is above 22 GPa for the highly oriented pyrolytic graphite to transform into hexagonal diamond, and a value higher than 46 GPa is required to transform the as-deposited pyrolytic graphite into cubic diamond.<sup>27</sup> On the other hand, graphite is more energetically stable than diamond, which leads to the tendency of carbon allotropes with an initial hexagonal-like configuration to adopt a planar structure rather than a buckled one. This results in the transformation of the initial C<sub>8</sub> into a graphite-like structure when it undergoes relaxation under ambient pressure.

To examine the possibility of synthesizing diamond through a denitrifying reaction in C<sub>1</sub>N<sub>1</sub>, the thermodynamic properties are investigated by calculating the dependence of formation enthalpy on pressure. In an experiment,<sup>20</sup> a platinum (Pt) or an iridium (Ir) ring spacer is employed and exposed to N<sub>2</sub>. Additionally, PtN, PtN<sub>2</sub> and IrN<sub>2</sub> were synthesized under high temperature and pressure conditions,<sup>29,30</sup> and carbon nitride was successfully denitrified in the presence of magnesium (Mg) by Yuan *et al.*<sup>31</sup> Therefore, the formation enthalpy is defined as:

$$\Delta H = \frac{mH^C + H^{M_nN_m} - mH^{C_1N_1} - nH^M}{2m + n}, \quad (1)$$

where  $H^C$  and  $H^{C_1N_1}$  are the enthalpy of diamond and C<sub>1</sub>N<sub>1</sub>,  $M$  represents the different types of metals, and  $H^{M_nN_m}$  and  $H^M$  are the enthalpy of the metal nitrides and metal crystals,

respectively. The results presented in Fig. 2(a) show that synthesizing diamond is experimentally feasible under the ambient conditions, in that the sum of total energy of diamond and PtN<sub>2</sub> or IrN<sub>2</sub> should be lower than those of the corresponding precursors. In the whole pressure range, the products diamond and PtN<sub>2</sub> remain thermodynamically stable. Whereas the products diamond and IrN<sub>2</sub> become thermodynamically unstable when the pressure is above ~20 GPa, in that  $\Delta H$  increases with increasing pressure and becomes positive above 20 GPa. When taking C<sub>1</sub>N<sub>1</sub> and Mg as precursors,  $\Delta H$  decreases as the pressure increases and remains negative throughout the entire pressure range. Importantly,  $\Delta H$  of this reaction is significantly lower than those of the other reactions, indicating that the denitrifying reaction in carbon nitrides is more easily promoted in the presence of Mg as compared to Pt or Ir.

Subsequently, a series of C<sub>1+x</sub>N<sub>1-x</sub> systems are studied through replacing different numbers of N atoms with C atoms. The initial structures are plotted in the left side of Fig. 3, and named as C<sub>5</sub>N<sub>3</sub>, C<sub>6</sub>N<sub>2</sub>-I, C<sub>6</sub>N<sub>2</sub>-II, C<sub>6</sub>N<sub>2</sub>-III, and C<sub>7</sub>N<sub>1</sub>, respectively. Then, the structures are relaxed at 0 and 70 GPa, respectively, and the optimized ones are drawn in the middle of Fig. 3. After relaxation under both pressures, the 3D-bonded framework of C<sub>1</sub>N<sub>1</sub> remains intact in C<sub>5</sub>N<sub>3</sub>, i.e., the C–C bonds between adjacent layers remain unbroken, and no new bonds are formed to link them. This performance can be elucidated by the mechanism below. The three-fold coordinated N and C atoms in the adjacent layers, indicated by the red arrows in Fig. 3, are unable to form N–C bonds due to the preference of N atoms to be three-fold coordinated. Half of the carbon atoms in the C–C bonds that connect the two adjacent layers are three-fold coordinated with nitrogen atoms, resulting in sp<sup>3</sup> hybridization of these carbon atoms (*i.e.*, forming bonds with carbon atoms in the adjacent layer in order to achieve four-fold coordination). However, breaking these C–C bonds will result

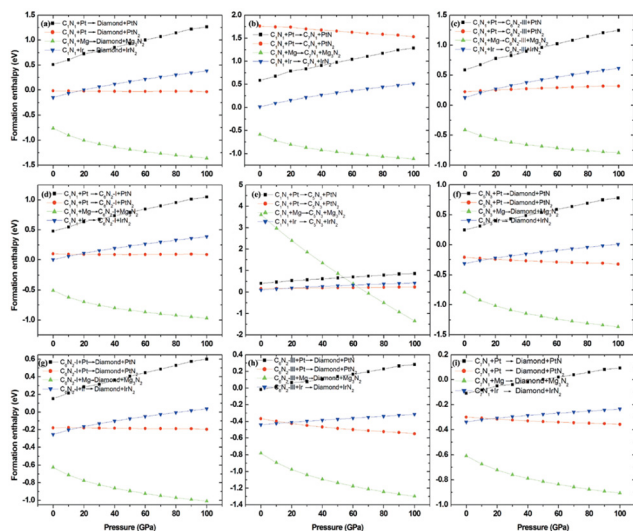


Fig. 2 The relationship between formation enthalpy and pressure in various denitrifying reactions.

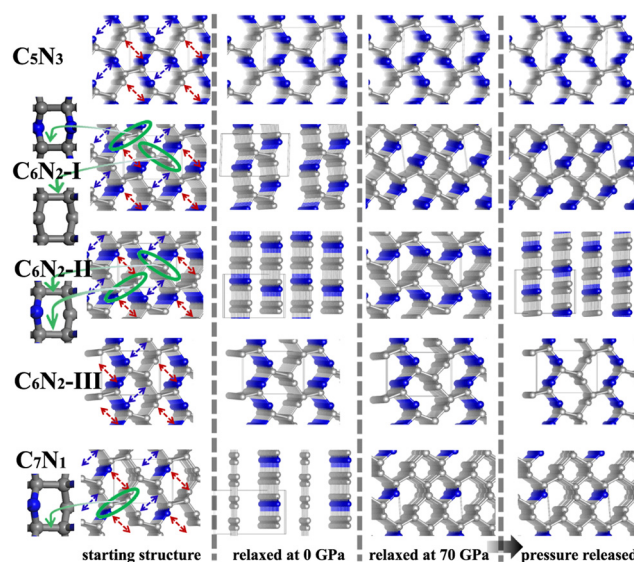


Fig. 3 The initial and optimized structures of C<sub>1+x</sub>N<sub>1-x</sub> systems. The inset on the left side is the views of hexatomic rings in the systems.



in the formation of numerous dangling bonds, which are energetically unfavorable. The structure of the  $C_6N_2$ -I phase transforms into a two-dimensional (2D) nanosheet layered crystal when relaxed at 0 GPa, but it becomes 3D-bonded at 70 GPa. It is clear that the strength of C–C bonds connecting the adjacent nanosheets varies. One type of C–C bonds is located in a carbon hexatomic ring. The other type of C–C bonds is situated on hexatomic rings consisting of both C and N atoms, which makes them much weaker due to the relatively larger electronegativity of N atoms. At 0 GPa, the weaker C–C bonds break and form double C–C bonds in nanosheets, while the stronger C–C bonds remain intact. This results in a layered configuration consisting of two interconnected  $C_6N_2$  layers. Under a high external pressure of 70 GPa, the three-fold coordinated ( $sp^2$  hybridized) carbon atoms (indicated by the blue arrows in Fig. 3) undergo a transition to four-fold coordination ( $sp^3$  hybridization), leading to the formation of C–C bonds that connect the adjacent layers. This transformation is analogous to the conversion from graphite to cubic diamond. With the release of pressure, the 3D-bonded structure remains. For the  $C_6N_2$ -II phase, the C–C bonds are weak due to coordination of C atoms with N atoms. Thus, the C 2p electrons prefer to form C–C double bonds in the nanosheet plane, similar to the  $C_6N_2$ -I phase at ambient pressure. According to the fact that the N atoms are three-fold coordinated, no new bonds could be formed between the corresponding atoms (represented by the blue and red arrows in Fig. 3) even at high pressure. Consequently, the relaxed structure undergoes a transformation into a layered configuration upon the release of pressure into the ambient environment. For  $C_6N_2$ -III, the initial structure could be regarded as the stacking of monolayered  $C_1N_1$  and graphene. In the monolayered  $C_1N_1$ , all carbon atoms are coordinated to three nitrogen atoms, resulting in the presence of the unpaired C 2p electrons. Thus, the system is energetically favorable by preserving the initial C–C bonds, regardless of pressure. For  $C_7N_1$ , the structure would turn into a 2D configuration at 0 GPa, similar to  $C_6N_2$ -II. Under high pressure, the C atoms that are three-fold coordinated (indicated by the blue arrows) prefer to form bonds, and this 3D-bonded structure persists even when the pressure is released to 0 GPa, similar to  $C_6N_2$ -I. The formation of bonds in the four 3D-bonded systems (in an ambient environment) can be confirmed by the electron localization functions (ELFs) as depicted in Fig. 4(a) and (b). It obviously shows that the neighboring atoms are bonded mainly with the  $\sigma$  state. The above result can also be proved by the charge density difference as shown in Fig. 4c. The formation of C–C bonds between the adjacent sublayers is evident from the accumulation of electrons. To further investigate the covalency of the bonds, Bader charges were calculated to assess the charge transfer, and the data are listed in Table 1. It is evident that there is minimal electron transfer between the atoms, attributed to the similar electronegativity of C and N atoms. This performance indicates a high level of bond covalency.

Some structural parameters for the  $C_5N_3$ ,  $C_6N_2$ -I,  $C_6N_2$ -III, and  $C_7N_1$  systems are given in Table 2.  $C_5N_3$ ,  $C_6N_2$ -I, and  $C_7N_1$

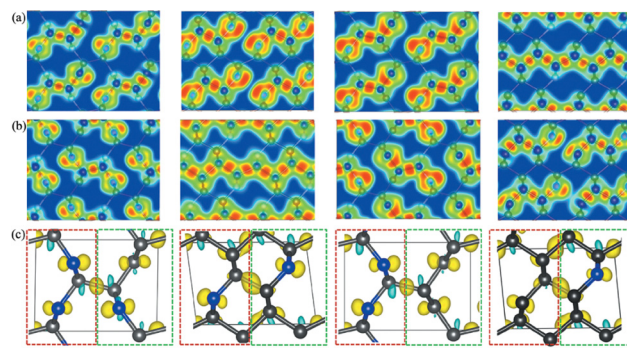


Fig. 4 (a) and (b) The electron localization functions (ELF) for the  $C_5N_3$ ,  $C_6N_2$ -I,  $C_6N_2$ -III, and  $C_7N_1$  systems of the two different (001) planes, respectively. (c) The charge density difference for the four  $C_5N_3$ ,  $C_6N_2$ -I,  $C_6N_2$ -III, and  $C_7N_1$  systems. The isosurface value is set to be  $0.001 \text{ e } \text{\AA}^{-3}$ . The electron accumulation and depletion regions are indicated by yellow and cyan, respectively. The charge density difference is expressed as  $\Delta\rho = \rho_{C_nN_m} - \rho_{\text{sublayer1}} - \rho_{\text{sublayer2}}$ . Sublayer1 and sublayer2 are displayed by rectangles with dashed red and green lines, respectively.

exhibit monoclinic crystals with  $Pm$ ,  $P2_1/m$ , and  $Pm$  symmetries, respectively.  $C_6N_2$ -III shows orthorhombic crystals with  $Pmn2_1$  symmetry. This demonstrates that substituting N atoms with C atoms alters the initial crystal symmetry of  $Pnnm$   $C_1N_1$ . The lattice parameters  $a$ ,  $b$  and  $c$  change significantly as well, for instance, both  $a$  and  $c$  increase after substitution. The relatively shorter C–C bonds are formed in the systems with values of  $\sim 1.47 \text{ \AA}$ , much shorter than  $\sim 1.58 \text{ \AA}$  in  $Pnnm$   $C_1N_1$ . This is attributed to the formation of C–C double bonds resulting from the substitution of N atoms with C atoms. In contrast,  $Pnnm$   $C_1N_1$  has only C–C single bonds due to the four-fold coordination of all C atoms. Besides, these lengths are longer than  $\sim 1.42 \text{ \AA}$  of the bonds in graphene, but shorter than  $\sim 1.55 \text{ \AA}$  of the C–C single bonds in diamond. This is because nitrogen atoms have a higher electronegativity, causing electrons to transfer to nitrogen atoms and weakening the strength of C–C double bonds. The C–C bonds connecting the adjacent layers have a length of  $\sim 1.61 \text{ \AA}$ , larger than  $\sim 1.58 \text{ \AA}$  in  $C_1N_1$ . The three-fold coordinated C atoms prefer to construct a flat 2D layered structure, which results in an elongation of the interlayer distance.

The presence of three-fold coordination of carbon atoms in the  $C_{1+x}N_{1-x}$  systems potentially induces unpaired electrons, which may contribute to the excitation of magnetism. The structures of the  $C_5N_3$ ,  $C_6N_2$ -III, and  $C_7N_1$  systems reveal the presence of three-fold coordinated carbon atoms that are not bonded to one another. This suggests that there are unpaired electrons in these systems. In the  $C_6N_2$ -I system, all the C atoms are four-fold coordinated, implying that all of their electrons are bonded. This suggests that the  $C_5N_3$ ,  $C_6N_2$ -III, and  $C_7N_1$  systems may exhibit magnetic ordering, while the  $C_6N_2$ -I system is in a nonmagnetic phase. Consequently, the ferromagnetic (FM), antiferromagnetic (AFM) and nonmagnetic (NM) phases are investigated to determine the ground-state phases of these  $C_{1+x}N_{1-x}$  systems. The total energies of these phases are calculated and presented in Table 3. As assumed, the antiferromagnetic phases of both  $C_5N_3$  and  $C_7N_1$  compounds

**Table 1** The calculated charge transfer in |e|

Phase	C1	C2	C3	C4	C5	C6	C7	N1	N2	N3
C <sub>5</sub> N <sub>3</sub>	0.05	0.05	0.06	0.04	−0.03	—	—	−0.03	−0.11	−0.03
C <sub>6</sub> N <sub>2</sub> -I	0.05	0.05	0.00	0.00	0.04	0.04	—	−0.09	−0.09	—
C <sub>6</sub> N <sub>2</sub> -III	0.06	0.07	0.06	0.06	−0.06	−0.06	—	−0.06	−0.06	—
C <sub>7</sub> N <sub>1</sub>	0.02	0.04	0.03	0.10	−0.05	0.17	−0.09	—	−0.03	—

**Table 2** The symmetry, lattice parameters *a*, *b*, *c*, and lengths of C–C and C–N bonds (Å) for C<sub>5</sub>N<sub>3</sub>, C<sub>6</sub>N<sub>2</sub>-I, C<sub>6</sub>N<sub>2</sub>-III, C<sub>7</sub>N<sub>1</sub>, C<sub>1</sub>N<sub>1</sub>, graphene (Gra), and cubic diamond (Dia), respectively

Bond	C <sub>5</sub> N <sub>3</sub>	C <sub>6</sub> N <sub>2</sub> -I	C <sub>6</sub> N <sub>2</sub> -III	C <sub>7</sub> N <sub>1</sub>	C <sub>1</sub> N <sub>1</sub>	Gra	Dia
C–C	1.46–1.61	1.52–1.62	1.47–1.60	1.47–1.62	1.58	1.42	1.55
C–N	1.45–1.50	1.43–1.45	1.46–1.47	1.46/1.50	1.42/1.47	—	—
Symm	<i>Pm</i> (no. 6)	<i>P2/m</i> (no. 10)	<i>Pmn21</i> (no. 31)	<i>Pm</i> (no. 6)	<i>Pnnm</i> (no. 58)	—	—
<i>a</i>	5.37	5.29	5.56	5.27	5.26	—	—
<i>b</i>	3.97	3.65	3.86	3.65	3.93	—	—
<i>c</i>	2.41	2.43	2.45	2.49	2.37	—	—

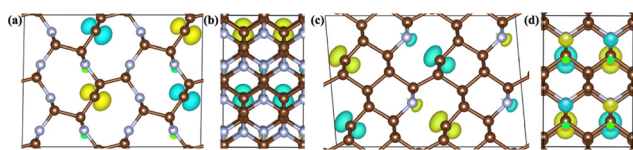
**Table 3** The total energies (eV per unit cell) of FM, AFM, and NM C<sub>5</sub>N<sub>3</sub>, C<sub>6</sub>N<sub>2</sub>-I, C<sub>6</sub>N<sub>2</sub>-III, and C<sub>7</sub>N<sub>1</sub> systems in an ambient environment, respectively. The total energies of NM phases are shifted to zero

Phase	C <sub>5</sub> N <sub>3</sub>	C <sub>6</sub> N <sub>2</sub> -I	C <sub>6</sub> N <sub>2</sub> -III	C <sub>7</sub> N <sub>1</sub>
FM	−1.24	0	0	−0.03
AFM	−1.34	0	0	−0.43
NM	0.00	0	0	0.00

have the lowest total energies, at least 0.10 and 0.40 eV per cell lower than the other magnetic phases. This demonstrates that the ground states of both systems are antiferromagnetically coupled. The magnetic moments are located on the C atoms with three-fold coordinated, as evidenced by the net magnetic charge density (*i.e.*, the electronic charge density difference between the spin-up and spin-down channels) in Fig. 5. The magnetic moment values on the corresponding atoms for the C<sub>5</sub>N<sub>3</sub> and C<sub>7</sub>N<sub>1</sub> systems are about 0.39 and 0.34 μ<sub>B</sub>, respectively. For C<sub>6</sub>N<sub>2</sub>-I and C<sub>6</sub>N<sub>2</sub>-III systems, both the spin-polarized and spin-unpolarized calculations yield a nonmagnetic characteristic, indicating that their ground-states are nonmagnetic. This suggests the unpaired electrons in C<sub>6</sub>N<sub>2</sub>-III are delocalized.

The magnetic transition temperature significantly influences the applications of materials. Therefore, the Néel temperature (*T<sub>c</sub>*) of the two magnetic phases, C<sub>5</sub>N<sub>3</sub> and C<sub>7</sub>N<sub>1</sub>, is approximately estimated by the mean-field approximation through the following expression,<sup>32</sup>

$$3/2k_{\text{B}}T_{\text{N}} = (E_{\text{AFM}} - E_{\text{FM}})/N \quad (2)$$

**Fig. 5** The 3D isosurface plots of magnetic charge density for the two AFM C<sub>5</sub>N<sub>3</sub> (a) and (b) and C<sub>7</sub>N<sub>1</sub> (c) and (d) phases, respectively. (a)–(d) The views from *a* and *c* directions, respectively.

where *N* is the number of magnetic atoms in the unit cell, *k<sub>B</sub>* is the Boltzmann constant, and *E<sub>FM</sub>* and *E<sub>AFM</sub>* represent the total energies per unit cell for the ferromagnetic and antiferromagnetic phases, respectively. The estimated *T<sub>N</sub>* values are 96 K for the C<sub>5</sub>N<sub>3</sub> and 386 K for the C<sub>7</sub>N<sub>1</sub> phases. Significantly, *T<sub>N</sub>* of the C<sub>7</sub>N<sub>1</sub> phase exceeds room temperature, suggesting its suitability for operation under ambient conditions.

To investigate the feasibility of synthesizing C<sub>1+x</sub>N<sub>1−x</sub> systems *via* a denitriding reaction between C<sub>1</sub>N<sub>1</sub> and Pt/Ir/Mg metals, the thermodynamic stability of C<sub>1+x</sub>N<sub>1−x</sub> is explored through formation enthalpy as given below

$$\Delta H = \frac{mH^{C_{1+x}N_{1-x}} + 2xH^{M_nN_m} - (1+x)mH^{C_1N_1} - 2n_xH^M}{2x(m+n) + 2m}, \quad (3)$$

where *H<sup>C<sub>1+x</sub>N<sub>1−x</sub></sup>* is the enthalpy of C<sub>1+x</sub>N<sub>1−x</sub> systems. The results are depicted in Fig. 2(b)–(e). It clearly shows that all C<sub>1+x</sub>N<sub>1−x</sub> systems are experimentally feasible in the presence of Mg, since all the formation enthalpy Δ*H* values are negative across the whole pressure range, except that of the reaction to obtain C<sub>5</sub>N<sub>3</sub>. Besides, all Δ*H* values have the same tendency, decreasing with increasing external pressure. For the C<sub>5</sub>N<sub>3</sub> system, Δ*H* becomes negative as long as the pressure is above ~60 GPa. Taking C<sub>1</sub>N<sub>1</sub> and Ir as precursors, C<sub>1+x</sub>N<sub>1−x</sub> systems are hard to synthesize, since all the Δ*H* values are positive and increase with increasing pressure. When choosing C<sub>1</sub>N<sub>1</sub> and Pt as reagents, although all the Δ*H* values are positive in the whole pressure range, they decrease as the pressure increases in C<sub>7</sub>N<sub>1</sub> and C<sub>6</sub>N<sub>2</sub>-I systems. This case suggests that C<sub>7</sub>N<sub>1</sub> and C<sub>6</sub>N<sub>2</sub>-I systems may become thermodynamically stable when the external pressure exceeds a critical value. In addition, the formation enthalpy plotted in Fig. 2(f)–(i) demonstrates the experimental feasibility of synthesizing diamond *via* a denitriding reaction between C<sub>1+x</sub>N<sub>1−x</sub> systems and all three metals.

Additionally, the formation enthalpy is calculated by utilizing graphite and N<sub>2</sub> as precursors, and Δ*H* is expressed as:

$$\Delta H = H^{C_{1+x}N_{1-x}} - (1+x)H^C - (1-x)H^N, \quad (4)$$

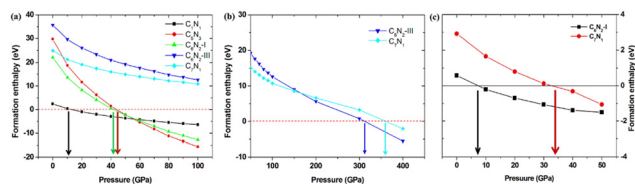


**Fig. 6** (a) The pressure-dependent formation enthalpies of the  $C_1N_1$ ,  $C_5N_3$ ,  $C_6N_2$ -I,  $C_6N_2$ -III, and  $C_7N_1$  systems with pressure from 0 to 100 GPa, respectively. (b) The pressure-dependent formation enthalpies of  $C_6N_2$ -III and  $C_7N_1$  systems with the pressure ranging from 100 to 400 GPa. (c) The pressure-dependent formation enthalpies of  $C_6N_2$ -I and  $C_7N_1$  using the 2D layered nanosheets as precursors.

where  $H^N$  represents the enthalpy of carbon diamond and the stable  $\alpha$  phase of nitrogen. The results are shown in Fig. 6. It clearly shows that all systems have positive formation energies under ambient conditions, suggesting that the systems are metastable compared to the precursors at 0 GPa. The dependence of formation enthalpy on the pressure is studied as well, as external pressure typically induces phase transformation. The  $Pnnm$   $C_1N_1$  system would become thermodynamically stable above  $\sim 11$  GPa, which is consistent with 10.9 GPa predicted by Wang.<sup>15</sup> The transition pressure increases with increasing C ratio, reaching 42, 45, 310, and 320 GPa for  $C_6N_2$ -I,  $C_5N_3$ ,  $C_6N_2$ -III, and  $C_7N_1$  systems, respectively. This fact suggests that it is possible to synthesize various  $C_{1+x}N_{1-x}$  systems under different critical pressures by utilizing diamond and the  $\alpha$  phase of nitrogen as reagents. However, as the C ratio increases, the synthesis conditions become more challenging. Additionally, the  $C_{1+x}N_{1-x}$  systems can be considered as being stacked with 2D nanosheets, and the transition pressure is significantly influenced by the precursors. Therefore, the corresponding 2D nanosheets are selected as precursors to investigate the transition pressure from a layered structure to a 3D-bonded structure, and  $C_6N_2$ -I and  $C_7N_1$  were selected as representatives. The results show that the transition pressures for  $C_6N_2$ -I and  $C_7N_1$  systems are about 7 and 34 GPa, respectively, which are relatively lower compared to the above values.

In many applications, it is essential for materials to maintain stability in an ambient environment. Therefore, the dynamic stability of these  $C_{1+x}N_{1-x}$  systems under ambient pressure is studied, and the corresponding phonon dispersion curves are presented in Fig. 7. It obviously shows that there are no imaginary phonon frequencies for all the systems. The phonon density of states is consistent with the phonon dispersion curves, *i.e.*, there are no states below zero. The absence of imaginary phonon frequencies demonstrates that the systems are dynamically stable under ambient pressure. Usually, a higher frequency indicates the presence of stronger bonds in materials. The highest frequencies, as shown in Fig. 7(g), are 1382, 1402, 1400, and 1368  $\text{cm}^{-1}$  for  $C_5N_3$ ,  $C_6N_2$ -I,  $C_6N_2$ -III, and  $C_7N_1$ , respectively. All these values are smaller than 1415  $\text{cm}^{-1}$  of  $C_1N_1$ , due to certain shorter or stronger C–N bonds in  $C_1N_1$  compared to those of the other  $C_{1+x}N_{1-x}$  systems. However, these frequencies are much higher than 1346  $\text{cm}^{-1}$  of the carbon diamond, because some C–C bonds in these  $C_{1+x}N_{1-x}$

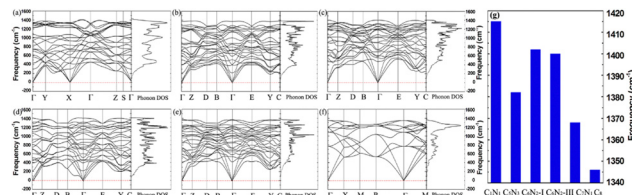


**Fig. 7** (a) The phonon-dispersion curves and phonon density of states for the  $Pnnm$   $C_1N_1$  phase. (b)–(e) The phonon-dispersion curves and phonon density of states for the  $C_5N_3$ ,  $C_6N_2$ -I,  $C_6N_2$ -III, and  $C_7N_1$  systems at ambient pressure. (f) The phonon-dispersion curves and phonon density of states for the diamond. (g) The highest phonon frequencies for  $C_1N_1$ ,  $C_5N_3$ ,  $C_6N_2$ -I,  $C_6N_2$ -III,  $C_7N_1$ , and carbon diamond ( $C_8$ ).

systems are much shorter or stronger than those in carbon diamond.

Mechanical stability is another crucial factor in the application of materials and is investigated for all  $C_{1+x}N_{1-x}$  systems. The mechanical stability criterion is given by the following expression for all crystals, *i.e.*, each order determinant of the elastic modulus matrix should be positive:

$$|c_{11}| > 0$$

$$\begin{vmatrix} c_{11} & c_{12} \\ c_{21} & c_{22} \end{vmatrix} > 0$$

.....

$$\begin{vmatrix} c_{11} & c_{12} & c_{13} & c_{14} & c_{15} & c_{16} \\ c_{12} & c_{22} & c_{23} & c_{24} & c_{25} & c_{26} \\ c_{13} & c_{23} & c_{33} & c_{34} & c_{35} & c_{36} \\ c_{14} & c_{24} & c_{34} & c_{44} & c_{45} & c_{46} \\ c_{15} & c_{25} & c_{35} & c_{45} & c_{55} & c_{56} \\ c_{16} & c_{26} & c_{36} & c_{46} & c_{56} & c_{66} \end{vmatrix} > 0$$

For the orthorhombic symmetry, there are nine independent elastic constants:  $C_{11}$ ,  $C_{22}$ ,  $C_{33}$ ,  $C_{44}$ ,  $C_{55}$ ,  $C_{66}$ ,  $C_{12}$ ,  $C_{13}$ , and  $C_{23}$ . These constants should satisfy the following six necessary and sufficient expressions:  $C_{11} > 0$ ,  $C_{11}C_{22} > C_{12}^2$ ,  $C_{11}C_{22}C_{33} + 2C_{12}C_{13}C_{23} - C_{11}C_{23}^2 - C_{22}C_{13}^2 - C_{33}C_{12}^2 > 0$ ,  $C_{44} > 0$ ,  $C_{55} > 0$ ,  $C_{66} > 0$ . For the monoclinic symmetry, it possesses thirteen independent elastic constants ( $C_{11}$ ,  $C_{22}$ ,  $C_{33}$ ,  $C_{44}$ ,  $C_{55}$ ,  $C_{66}$ ,  $C_{12}$ ,  $C_{13}$ ,  $C_{23}$ ,  $C_{15}$ ,  $C_{25}$ ,  $C_{35}$ , and  $C_{46}$ ) which should satisfy the following five necessary and sufficient expressions:  $C_{11} > 0$ ,  $C_{22} > 0$ ,  $C_{33} > 0$ ,  $C_{44} > 0$ ,  $C_{55} > 0$ ,  $C_{66} > 0$ ,  $C_{11} + C_{22} + C_{33} + 2(C_{12} + C_{13} + C_{23}) > 0$ ,  $C_{33}C_{55} - C_{35}^2 > 0$ ,  $C_{44}C_{66} - C_{46}^2 > 0$ ,  $C_{22} + C_{33} - 2C_{23} > 0$ ,  $C_{22}(C_{33}C_{55} - C_{35}^2) + 2C_{23}C_{25}C_{35} - C_{23}^2C_{55} - C_{25}^2C_{33} > 0$ ,  $2[C_{15}C_{25}(C_{33}C_{12}) - C_{13}C_{23} + C_{15}C_{35}(C_{22}C_{13} - C_{12}C_{23}) + C_{25}C_{35}(C_{11}C_{23} - C_{12}C_{13})] - [C_{15}^2(C_{22}C_{33} - C_{23}^2) + C_{25}^2(C_{11}C_{33} - C_{13}^2) + C_{35}^2(C_{11}C_{22} - C_{12}^2)] + C_{55}g > 0$ .  $g = C_{11}C_{22}C_{33} - C_{11}C_{23}^2 - C_{22}C_{13}^2 - C_{33}C_{12}^2 + 2C_{12}C_{13}C_{23}$ .

In order to evaluate the accuracy and validity of the method used, the mechanical properties of diamond are initially

calculated first, and the results are listed in Table 3. The calculated elastic stiffness constants are in good agreement with the experimental data.<sup>33,34</sup> Next, the elastic stiffness constants of the  $C_{1+x}N_{1-x}$  systems are calculated and given in Table 3. Consequently, the elastic stiffness constants of all systems satisfy the mechanical criteria, indicating their mechanical stability.

Elastic deformation is important for the applications of materials. Furthermore, various moduli that reflect a material's intrinsic response to different types of deformations, including bulk modulus ( $B$ ), shear modulus ( $G$ ), Young's modulus ( $E$ ), Poisson's ratio ( $\nu$ ), Pugh's ratio ( $p$ ), *etc.*, are explored. The Voigt–Reuss–Hill approximations<sup>35</sup> are used to estimate these values. The calculated data are given in Table 4. The values of  $B$ ,  $G$ ,  $E$ , and  $\nu$  of diamond are in good agreement with the experimental values, confirming the reliability of our results. The moduli  $B$ ,  $G$ , and  $E$  of the  $C_{1+x}N_{1-x}$  systems are much smaller than those of diamond, primarily because of their porous structure. Poisson's ratios ( $\nu$ ) of all the  $C_{1+x}N_{1-x}$  systems are about 0.15, much larger than 0.07 of diamond. Usually, Poisson's ratio  $\nu$  reflects the strength of covalent bonding in a material, and it is typically less than 0.10 for covalently bonded materials. This suggests that the covalent bonds in the  $C_{1+x}N_{1-x}$  systems are weaker than those in diamond, primarily because of the electronegativity difference between carbon and nitrogen atoms. Additionally, the presence of relatively weak covalent bonds results in a smaller shear modulus (Table 5).

Pugh's ratio ( $B/G$ ) is used to assess the brittleness ( $B/G < 1.75$ ) or ductility ( $B/G > 1.75$ ) of materials.<sup>36</sup> The estimated values of Pugh's ratio for the  $C_{1+x}N_{1-x}$  systems are listed in Table 4. The Pugh's ratio of the systems ranges from 1.05 to 1.20, all of which are much higher than 0.83 of diamond. This implies that the  $C_{1+x}N_{1-x}$  systems might exhibit higher ductility in comparison to diamond. To validate this result, the hardness of the  $C_{1+x}N_{1-x}$  systems is investigated. Here, a common metrics  $H_V$  is estimated using both the Chen ( $H_V^C$ )<sup>37</sup> and Mazhnik–Oganov ( $H_V^{MO}$ )<sup>38</sup> models, as expressed in eqn (4) and (5):

$$H_V^C = (2((1/p)^2 G)^{0.585} - (3)) \quad (5)$$

$$H_V^{MO} = 0.096E(1 - 8.5\nu + 1.95\nu^2)/(1 - 7.5\nu + 12.2\nu^2 + 19.6\nu^3), \quad (6)$$

and the calculated data for the systems are drawn in Fig. 8(a). The calculated hardness of diamond under the two models is 92.6 and 98.5 GPa, respectively, which is consistent with the

**Table 5** The calculated bulk modulus  $B$  (GPa), shear modulus  $G$  (GPa), Young's modulus  $E$  (GPa), Poisson's ratio ( $\nu$ ), Pugh's ratio ( $p = B/G$ ), and transverse ( $\nu_t$ ) and longitudinal ( $\nu_l$ ) elastic wave velocities ( $m s^{-1}$ ) for the  $C_{1+x}N_{1-x}$  systems and diamond

Phases	$B$	$G$	$E$	$\nu$	$p$	$\nu_l$	$\nu_t$
Diamond	434	519	1114	0.07	0.83	17 910	12 175
Dia-Exp	422	534		0.07			
$C_1N_1$	360	341	778	0.14	1.05	15 184	9825
$C_5N_3$	275	245	567	0.15	1.12	13 511	8624
$C_6N_2$ -I	411	370	853	0.15	1.11	15 930	10 190
$C_6N_2$ -III	262	220	515	0.17	1.20	13 241	8327
$C_7N_1$	368	351	799	0.14	1.05	15 657	10 141

experimental value of 96.0 GPa.<sup>34</sup> The  $H_V^C$  and  $H_V^{MO}$  values of the  $C_1N_1$  system are 53.0 and 59.2 GPa, respectively, agreeing well with the value of 59.6 GPa reported by Stavrou *et al.*<sup>20</sup> The hardness of the other four  $C_{1+x}N_{1-x}$  systems varies between 35 and 54.5 GPa, which is considerably lower than 92.6 GPa of diamond, but similar to 53 GPa of  $C_1N_1$ . This performance is consistent with that of Pugh's ratio. These values are also lower than those of the other carbon nitrides with different C/N ratios, such as 62.3–92.0 GPa for  $C_3N_4$ ,<sup>14</sup> 64.0 GPa for  $C_{17}N_{11}$ ,<sup>17</sup> 82.0 GPa for the cubic CN with  $P2_13$  symmetry,<sup>39</sup> 58–68 GPa for  $C_3N_2$  with different symmetry,<sup>16,40</sup> *etc.* Besides, this hardness is also a bit smaller than 63.8 GPa of the other commercially applied c-BN. Notably,  $C_5N_3$  ( $H_V^C = 40.3$  GPa),  $C_6N_2$ -I ( $H_V^C = 52.6$  GPa), and  $C_7N_1$  ( $H_V^C = 54.5$  GPa) phases exhibit superhard nature, since all of their hardness are larger than 40 GPa. For the  $C_6N_2$ -III phase, it has a hardness of about 35 GPa, much lower than those of the other systems, although it still shows hard characteristic. Its relatively low hardness, compared to the other  $C_{1+x}N_{1-x}$  systems, is attributed to the existence of delocalized electrons that weaken the strength of bonds. To investigate the primary factors influencing the hardness of these  $C_{1+x}N_{1-x}$  systems, their mass density is calculated and presented in Fig. 8(a). It clearly shows that the mass density of these  $C_{1+x}N_{1-x}$  systems exhibits a similar trend to the hardness, demonstrating that the hardness of these  $C_{1+x}N_{1-x}$  systems primarily depends on their mass density. The mass density of  $C_5N_3$ ,  $C_6N_2$ -III, and  $C_7N_1$  is lower than 3.51 and 3.48  $g cm^{-3}$  of diamond and c-BN, and the relatively lower mass density originates from their porous structures. For the  $C_1N_1$  and  $C_6N_2$ -I systems, although they possess a higher mass density than those of diamond and c-BN, their reduced hardness is attributed to the weaker covalency of the bonds resulting from the different electronegativities of C and N atoms.

**Table 4** The calculated elastic stiffness constants of the  $C_{1+x}N_{1-x}$  and diamond. Dia-Exp is for the data of diamond from the experimental literature

Phases	$C_{11}$	$C_{12}$	$C_{13}$	$C_{23}$	$C_{22}$	$C_{33}$	$C_{44}$	$C_{55}$	$C_{66}$
Dia-Exp	1076	125					577		
Diamond	1052	125					560		
$C_1N_1$	546	218	83	144	697	1227	451	286	394
$C_5N_3$	458	212	46	93	377	1076	376	243	289
$C_6N_2$ -I	701	288	77	124	859	1217	441	315	441
$C_6N_2$ -III	507	204	83	84	272	1100	216	251	305
$C_7N_1$	698	213	54	112	824	1122	416	294	378

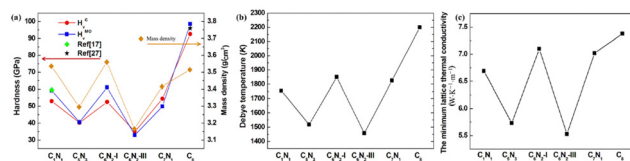


**Fig. 8** (a) The hardness and mass density for the  $C_{1+x}N_{1-x}$  systems and diamond. (b) and (c) The Debye temperature and the minimum lattice thermal conductivity for the  $C_{1+x}N_{1-x}$  systems and diamond, respectively.



Clearly, the Debye temperature ( $\theta_D$ ) is closely associated with various physical properties of materials, such as specific heat, elasticity, melting point, and hardness, *etc.* It is defined as

$$\theta_D = \frac{h}{k_B} \left[ \frac{3n}{4\pi} \left( \frac{N_A \rho}{M} \right) \right]^{1/3} v_m \quad (7)$$

where  $h$  represents Planck's constant,  $n$  is the atomic number of the molecule,  $N_A$  is Avogadro's number,  $\rho$  is the density of the molecule,  $k_B$  represents Boltzmann's constant,  $M$  is the molecular weight, and  $v_m$  denotes the average sound velocity.

$v_m$  is expressed as  $v_m = \left[ \frac{1}{3} \left( \frac{2}{v_t^3} + \frac{1}{v_l^3} \right) \right]^{-1/3}$ , where  $v_t$  and  $v_l$  are the transverse and longitudinal elastic wave velocities of solids

and calculated by using Navier's equations of  $v_t = \left( \frac{G}{\rho} \right)^{1/2}$  and

$v_l = \left( \frac{B + (4G/3)}{\rho} \right)^{1/2}$ . The calculated  $v_l$  and  $v_t$  values are given

in Table 4, and the  $\theta_D$  values are plotted in Fig. 8(b). The  $\theta_D$  value of the  $C_{1+x}N_{1-x}$  systems ranges from 1458 to 1826 K, greatly lower than 2200 K of diamond. Moreover, the Debye temperatures of these systems follow the same tendency as their hardness.

The thermal conductivity of these systems is also investigated, as it is another crucial factor for materials working at high temperatures. Therefore, the minimum lattice thermal conductivity is estimated using the Cahill's formula:<sup>41</sup>

$$k_{\min} = \frac{k_B}{2.48} n^{2/3} (2v_t + v_l), \quad (8)$$

where  $n$  represents the number density of atoms. The calculated values for the systems are shown in Fig. 8(c). For the  $C_5N_3$  and  $C_6N_2$ -III phases, the  $k_{\min}$  values are  $\sim 5.73$  and  $\sim 5.53$   $\text{W K}^{-1} \text{m}^{-1}$ , greatly lower than 6.69 and 7.37  $\text{W K}^{-1} \text{m}^{-1}$  of  $C_7N_1$  and diamond. For the  $C_6N_2$ -I and  $C_7N_1$  phases, the  $k_{\min}$  values are 7.10 and 7.02  $\text{W K}^{-1} \text{m}^{-1}$ , much higher than 6.69  $\text{W K}^{-1} \text{m}^{-1}$  of  $C_7N_1$ , but lower than 7.37  $\text{W K}^{-1} \text{m}^{-1}$  of diamond. The thermal conductivity tendency of these systems can be explained by their hardness, and materials with higher hardness usually possess higher thermal conductivity. It can be clearly concluded from Fig. 8 that the hardness, Debye temperature, and minimum lattice thermal conductivity of the systems exhibit a similar trend.

It is well known that Poisson's ratio  $\nu$  generally reflect the conductivity of materials, *i.e.*, materials with higher  $\nu$  typically exhibit greater conductivity. To further explore the electronic properties of the  $C_{1+x}N_{1-x}$  systems, the band structures, density of electronic states (DOS), and partial density of electronic states (PDOS) of the systems are investigated and shown in Fig. 9. As predicted, the three superhard phases  $C_5N_3$ ,  $C_6N_2$ -I, and  $C_7N_1$  behave as semiconductors. The hard phase  $C_6N_2$ -III exhibits metallic properties. This is consistent with the existence of the delocalized unpaired electron on three-fold coordinated carbon atoms. The band gaps are about 0.3, 0.79, and 0.20 eV for the  $C_5N_3$ ,  $C_6N_2$ -I, and  $C_7N_1$  systems, respectively. Considering the fact that the PBE functional would generally

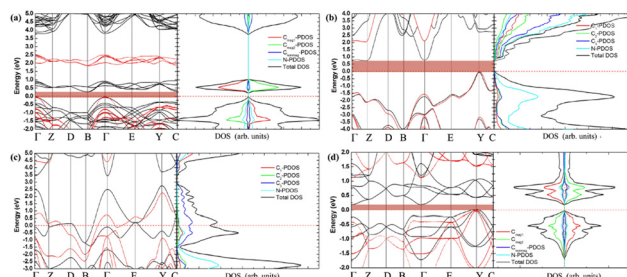


Fig. 9 (a)–(d) The band structures, total density of electronic states, and partial density of electronic states (PDOS) for  $C_5N_3$ ,  $C_6N_2$ -I,  $C_6N_2$ -III, and  $C_7N_1$ , respectively. For the  $C_6N_2$ -I system in (b),  $C_1$  is the C atoms coordinated by four C atoms,  $C_2$  is the C atoms coordinated by three C atoms and one N atom,  $C_3$  is the C atoms bonded to two N and two C atoms, as indicated by a green elliptic solid line in Fig. 2. For the  $C_6N_2$ -III system in (c),  $C_1$  represents the C atoms coordinated by four C atoms,  $C_2$  represents the C atoms coordinated by one C atom and three N atoms,  $C_3$  represents the three-fold coordinated C atoms. The black and red lines in the band structures present results given by the PBE and HSE functionals, respectively.

underestimate the band gap, the screened hybrid functional of Heyd, Scuseria, and Ernzerhof (HSE),<sup>42</sup> which typically provides more accurate band gaps compared to the PBE functional, is employed additionally. The results show that the band gaps are about 1.80, 2.00, and 1.10 eV for the  $C_5N_3$ ,  $C_6N_2$ -I, and  $C_7N_1$  systems, respectively. The  $C_6N_2$ -III phase still exhibits metallic behavior. These gaps are much smaller than those of traditional superhard materials (*e.g.*,  $\sim 5.60$  eV of diamond,  $\sim 6.40$  eV of c-BN), and they are also smaller than  $\sim 3.70$  eV of  $C_{11}N_1$ .<sup>15</sup> Therefore, these systems could address the gap in superhard materials with small band gaps or metallic features. Moreover, all of the systems behave as indirect band gap semiconductors, since the valence band maximum (VBM) and the conduction band minimum (CBM) are located at the different reciprocal lattice points. This case is the same as those of diamond, c-BN, and  $C_{11}N_1$ .

The total DOS of  $C_{1+x}N_{1-x}$  systems are consistent with the band structures. There are no electronic states located at the Fermi energy level ( $E_F$ ) for the  $C_5N_3$ ,  $C_6N_2$ -I, and  $C_7N_1$  systems, and the energy gap corresponds to the values provided by the band structures. Some electronic states are situated at  $E_F$  for the  $C_6N_2$ -III system, indicating the metallic nature as revealed by the band structure. Furthermore, the PDOS reveals that, in the same spin channel, the valence and conduction bands of both the antiferromagnetic  $C_5N_3$  and  $C_7N_1$  systems are mainly attributed to 2p states of the three-fold coordinated C atoms with opposite magnetic moments. For the nonmagnetic  $C_6N_2$ -I system, the valence and conduction bands are mainly composed of both  $C_3$  and N 2p orbitals. For the nonmagnetic  $C_6N_2$ -III system, the electronic states at  $E_F$  are mainly composed of  $C_3$  2p orbitals.

Based on the fact that devices usually work under external pressure, therefore, it is essential to explore the effect of external pressure on the electronic structures and magnetic properties of these  $C_{1+x}N_{1-x}$  systems. Fig. 10(a) shows the dependence of enthalpy on the external pressure (ranging from



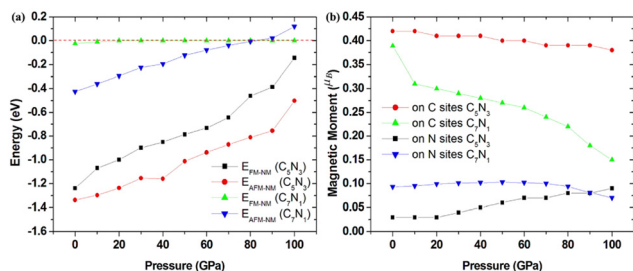


Fig. 10 (a) The pressure-dependent enthalpy difference between the AFM/FM and NM phases for the C<sub>5</sub>N<sub>3</sub> and C<sub>7</sub>N<sub>1</sub> systems. (b) The pressure-dependent magnetic moment on the corresponding atomic sites for the C<sub>5</sub>N<sub>3</sub> and C<sub>7</sub>N<sub>1</sub> systems.

0 to 100 GPa) of the C<sub>1+x</sub>N<sub>1-x</sub> systems. It is clear that the AFM phase of C<sub>5</sub>N<sub>3</sub> remains energetically stable in the whole pressure range, despite the enthalpy difference between the AFM and NM phases decreases with increasing external pressure. The AFM phase of C<sub>7</sub>N<sub>1</sub> is energetically favored when the pressure is below ~80 GPa, and then the NM phase becomes energetically stable. In addition, the AFM phases for both C<sub>5</sub>N<sub>3</sub> and C<sub>7</sub>N<sub>1</sub> systems are energetically stable than the FM ordering phases, except for the FM phase of C<sub>7</sub>N<sub>1</sub>, which becomes energetically stable when the pressure exceeds ~85 GPa. Fig. 10(b) illustrates the relationship between the magnetic moment and the external pressure. For the AFM C<sub>5</sub>N<sub>3</sub> system, the magnetic moment on C atoms decreases slightly from 0.42 to 0.38 μ<sub>B</sub>, while the magnetic moment on the N atoms increases slightly from 0.03 to 0.09 μ<sub>B</sub>. In the AFM C<sub>7</sub>N<sub>1</sub> system, the magnetic moment on C atoms decreases significantly from 0.39 to 0.15 μ<sub>B</sub>, and that on the N atoms decreases from 0.09 to 0.07 μ<sub>B</sub>. The difference in the trend of the magnetic moment between the two AFM systems can be primarily attributed to their distinct structural properties. The pore in C<sub>5</sub>N<sub>3</sub> is much larger than that in C<sub>7</sub>N<sub>1</sub>. Consequently, the overlap of the orbitals in C<sub>5</sub>N<sub>3</sub> would be much weaker than that in C<sub>7</sub>N<sub>1</sub> when subjected to external pressure. The greater overlap of orbitals would significantly weaken the magnetic moments, resulting in a faster decrease in magnetic moments in C<sub>7</sub>N<sub>1</sub> compared to C<sub>5</sub>N<sub>3</sub>.

Finally, the effect of external pressure on the band gaps of the three semiconducting systems is studied, and the corresponding results are shown in Fig. 11. Interestingly, the band

gap of the C<sub>5</sub>N<sub>3</sub> system increases from 0.30 to 0.50 eV (from 1.80 to 1.98 eV in the HSE level) as the pressure increases up to 50 GPa, and then the gap decreases to 0.35 eV (~1.91 eV in HSE level) as the pressure continues to increase up to 100 GPa. For the C<sub>6</sub>N<sub>2</sub>-I system, the band gap changes slightly and remains about 0.79 eV (~2.20 eV in HSE level), regardless of the external pressure. This changing behavior of the band gap under external pressure is scarce. It can be explained by the porous structure and superhardness of C<sub>5</sub>N<sub>3</sub> and C<sub>6</sub>N<sub>2</sub>-I systems, which lead to weak overlap of orbitals when external pressure is applied. For the C<sub>7</sub>N<sub>1</sub> system, the energy gap decreases from 0.20 eV to 0 eV as the pressure increases up to 50 GPa. A continuous increase in external pressure would cause the C<sub>7</sub>N<sub>1</sub> system to transform into a metal. The results from HSE show a similar trend. This performance is attributed to the significant orbital overlap resulting from external pressure, which is facilitated by its dense structure in comparison to the C<sub>5</sub>N<sub>3</sub> and C<sub>6</sub>N<sub>2</sub>-I systems.

## 4 Conclusions

In summary, with the help of first-principles calculations, various C<sub>1+x</sub>N<sub>1-x</sub> systems have been designed by replacing different numbers of N atoms with C atoms in the synthesized *Pnnm* C<sub>1</sub>N<sub>1</sub> system. Depending on the different replacement situations, they exhibit diverse physical properties, including magnetism, semiconductivity, superhardness, metallic behavior, *etc.* The presence of magnetism in C<sub>5</sub>N<sub>3</sub> and C<sub>7</sub>N<sub>1</sub> systems enriches the physical properties of superhard materials, which can expand their application into spintronic fields, *etc.* This case further confirms that the induction of three-fold coordinated C atoms is an effective method for synthesizing magnetic carbon-based superhard materials. For the C<sub>5</sub>N<sub>3</sub> and C<sub>6</sub>N<sub>2</sub>-I systems, their electronic structures are slightly affected by external pressure, making them highly advantageous for applications that require resisting the adverse effects caused by external pressure. This suggests that porous materials with superhardness can retain their physical properties when subjected to external pressure, in that the strong covalent bonds can effectively resist the structural deformation caused by stress. This provides a potential approach to designing materials whose physical properties are insensitive to external pressure. The narrow band gaps of C<sub>5</sub>N<sub>3</sub> and C<sub>7</sub>N<sub>1</sub> systems make them suitable for unique photoelectric applications that cannot be accomplished using conventional superhard materials, particularly in the mid-far-infrared fields. This work also demonstrates that reducing the coordination number of certain constituent atoms in light element systems is feasible to design magnetic superhard materials. We hope that experimental researchers will be able to synthesize these materials in the near future.

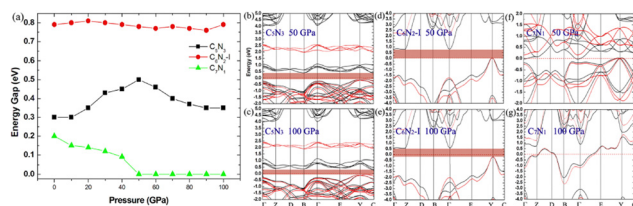


Fig. 11 (a) The pressure-dependent energy gap of C<sub>5</sub>N<sub>3</sub>, C<sub>6</sub>N<sub>2</sub>-I, and C<sub>7</sub>N<sub>1</sub> systems. (b)–(g) The band structures for the three systems under 50 and 100 GPa external pressures, respectively. The black and red lines in the band structures represent the results obtained from the PBE and HSE functionals, respectively.

## Data availability

Data are provided within the article.

## Author contributions

Haiping Wu: conceptualization, formal analysis, methodology, writing – review, and editing. Yunhao Zheng: investigation, computation, writing, and formal analysis. Erjun Kan: conceptualization, review, and formal analysis. Yan Qian: conceptualization, methodology, formal analysis, and review.

## Conflicts of interest

There are no conflicts to declare.

## Acknowledgements

This work was supported by the National Natural Science Foundation of China (Grant No. 12274226).

## Notes and references

- J. Haines, J. M. Leger and G. Bocquillon, *Annu. Rev. Mater. Res.*, 2001, **31**, 1–23.
- B. Xu and Y. Tian, *Sci. China: Mater.*, 2015, **58**, 132–142.
- R. B. Kaner, J. J. Gilman and S. H. Tolbert, *Science*, 2005, **308**, 1268–1269.
- A. Krauss, O. Auciello, D. Gruena, A. Jayatissa, A. Sumant, J. Tucek, D. Mancini, N. Moldovan, A. Erdemir, D. Ersoy, M. Gardos, H. Busmann, E. Meyer and M. Ding, *Diamond Relat. Mater.*, 2001, **10**, 1952.
- R. Wentorf, R. DeVries and F. Bundy, *Science*, 1980, **208**, 873.
- Z. Cui, H. Wu, K. Yang, X. Wang and Y. Lv, *Sens. Actuators, A*, 2024, **366**, 114954.
- Z. Cui, K. Yang, Y. Shen, Z. Yuan, Y. Dong, P. Yuan and E. Li, *Appl. Surf. Sci.*, 2023, **613**, 155978.
- D. Laniel, F. Trybel, A. Aslandukov, S. Khandarkhaeva, T. Fedotenko, Y. Yin, N. Miyajima, F. Tasnadi, A. V. Ponomareva, N. Jena, F. I. Akbar, B. Winkler, A. Neri, S. Chariton, V. Prakapenka, V. Milman, W. Schnick, A. N. Rudenko, M. I. Katsnelson, I. A. Abrikosov, L. Dubrovinsky and N. Dubrovinskaia, *Adv. Mater.*, 2023, 2308030.
- A. Y. Liu and M. L. Cohen, *Science*, 1989, **245**, 841–842.
- D. M. Teter and R. J. Hemley, *Science*, 1996, **271**, 53–55.
- A. Y. Liu and M. L. Cohen, *Phys. Rev. B: Condens. Matter Mater. Phys.*, 1990, **41**, 10727.
- A. Y. Liu and R. M. Wentzcovitch, *Phys. Rev. B: Condens. Matter Mater. Phys.*, 1994, **50**, 10362.
- C. M. Niu, Y. Z. Lu and C. M. Lieber, *Science*, 1993, **261**, 334.
- J. He, L. Guo, X. Guo, R. Liu, Y. Tian, H. Wang and C. Gao, *Appl. Phys. Lett.*, 2006, **88**, 101906.
- X. Wang, *J. Chem. Phys.*, 2012, **138**, 184506.
- F. Tian, J. Wang, Z. He, Y. Ma, L. Wang, T. Cui, C. Chen, B. Liu and G. Zou, *Phys. Rev. B: Condens. Matter Mater. Phys.*, 2008, **78**, 235431.
- Z. Li, K. Luo, B. Liu, L. Sun, P. Ying, C. Liu, W. Hu and J. He, *Carbon*, 2021, **184**, 846–854.
- J. Shao, Y. Qian, E. Kan and H. Wu, *J. Phys. D: Appl. Phys.*, 2023, **56**, 205303.
- H. Wu, Y. Li, Y. Qian and E. Kan, *Phys. Chem. Chem. Phys.*, 2023, **25**, 21408.
- E. Stavrou, S. Lobanov, H. Dong, A. R. Oganov, V. B. Prakapenka, Z. Konopkova and A. F. Goncharov, *Chem. Mater.*, 2016, **28**, 6925–6933.
- G. Kresse and J. Furthmüller, *Comput. Mater. Sci.*, 1996, **6**, 15–50.
- J. P. Perdew, K. Burke and M. Ernzerhof, *Phys. Rev. Lett.*, 1996, **77**, 3865.
- G. Kresse and D. Joubert, *Phys. Rev. B: Condens. Matter Mater. Phys.*, 1999, **59**, 1758.
- S. Baroni, S. Gironcoli, A. Corso and P. Giannozzi, *Rev. Mod. Phys.*, 2001, **73**, 515.
- K. Parlinski, Z. Li and Y. Kawazoe, *Phys. Rev. Lett.*, 1997, **78**, 4063.
- A. Togo, F. Oba and I. Tanaka, *Phys. Rev. B: Condens. Matter Mater. Phys.*, 2008, **78**, 134106.
- T. J. Volz and Y. M. Gupta, *Phys. Rev. B*, 2021, **103**, L100101.
- J.-T. Wang, C. Chen and Y. Kawazoe, *Phys. Rev. Lett.*, 2011, **106**, 075501.
- E. Gregoryanz, C. Sanloup, M. Somayazulu, J. Badro, G. Fiquet, H.-K. Mao and R. J. Hemley, *Nat. Mater.*, 2004, **3**, 294–297.
- J. C. Crowhurst, A. Goncharov, B. Sadigh, C. Evans, P. Morrall, J. Ferreira and A. Nelson, *Science*, 2006, **311**, 1275–1278.
- Y. Yuan, T. Wang, H. Chen, S. M. Mahurin, H. Luo, G. Veith, Z. Yang and S. Dai, *Angew. Chem., Int. Ed.*, 2020, **59**, 21935–21939.
- P. Kurz, G. Bihlmayer and S. Blugel, *J. Phys: Condens. Matter*, 2002, **14**, 6353.
- M. Grimsditch and A. Ramdas, *Phys. Rev. B: Condens. Matter Mater. Phys.*, 1975, **11**, 3139.
- R. A. Andrieviski, *Int. J. Refract. Met. Hard Mater.*, 2001, **19**, 447.
- H. Richard, *Proc. Phys. Soc. A*, 1952, **65**, 349.
- S. Pugh, *Philos. Mag. A*, 1954, **45**, 823.
- X. Chen, H. Niu, D. Li and Y. Li, *Intermetallics*, 2011, **19**, 1275.
- E. Mazhnik and A. Oganov, *J. Appl. Phys.*, 2019, **126**, 125109.
- X. Wang, K. Bao, F. Tian, X. Meng, C. Chen, B. Dong, D. Li, B. Liu and T. Cui, *J. Chem. Phys.*, 2010, **133**, 044512.
- J. Du and X. Li, *J. Alloys Compd.*, 2020, **815**, 152324.
- D. Cahill, S. Watson and R. Pohl, *Phys. Rev. B: Condens. Matter Mater. Phys.*, 1992, **46**, 6131–6140.
- J. Heyd, G. E. Scuseria and M. Ernzerhof, *J. Chem. Phys.*, 2003, **118**, 8207.